Designing dual-functional metal-organic frameworks for photocatalysis

Nan-Chieh Chiu,[a,b] Makenzie T. Nord,[a,b] Longteng Tang,[b] Logan S. Lancaster,[b] Jacob S. Hirschi,[b] Samuel K. Wolff,[a,b] Elan Maiti Hutchinson,[c] Konstantinos A. Goulas,[c] William F. Stickle,[d] Tim J. Zuehlsdorff,*[b] Chong Fang,*[b] Kyriakos C. Stylianou*[a,b]

[a]*Materials Discovery Laboratory (MaD Lab), 153 Gilbert Hall, Department of Chemistry, Oregon State University, Corvallis, OR 97331-4003 USA*

[b]*Department of Chemistry, Oregon State University, Corvallis, OR, 97331-4003 USA*

[c]*School of Chemical, Biological, and Environmental Engineering, Oregon State University, Corvallis, OR, 97331-4003 USA*

[d]*Hewlett-Packard Co., 1000 NE Circle Blvd., Corvallis, Oregon, 97330, United States*

E-mail: tim.zuehlsdorff@oregonstate.edu; chong.fang@oregonstate.edu; kyriakos.stylianou@oregonstate.edu

Abstract

Hydrogen (H_2) is an ideal alternative to fossil fuels as it is sustainable and environmentally friendly. Hydrogen production using semiconductor-based materials has been extensively investigated; most studies, however, rely on the use of sacrificial electron donors to consume the photogenerated holes, which wastes their oxidizing potential. Dual-functional photocatalysis (DFP) couples the production of H_2 with the oxidation of organic molecules, enabling simultaneous utilization of both photogenerated species. To develop efficient materials for DFP, herein, we investigate the interplay of electron/hole dynamics and photophysical properties of metal-organic frameworks (MOFs) using experimental and computational techniques. Four zirconium-based MOFs (UiO-66 analogs) were synthesized using different nitrogen-functionalized ligands. We used benzenethiol in place of a sacrificial reagent to enable simultaneous H_2 production and benzenethiol oxidation to sulfide-based products. We demonstrated that Pt/UiO-66-pz (Pt: platinum nanoparticles, pz: pyrazine) is the most efficient dual-functional photocatalyst as it achieved the highest H_2 production rates and second-best benzenethiol conversion. Our results shed light on the complex DFP process, wherein the interplay of light absorption, conductivity, band alignment, and charge separation and transfer capabilities are vital for enhancing the dual-functional photocatalytic activity of MOFs.

Introduction

The production of hydrogen fuel (H_2) using two abundant resources, water, and solar energy, is considered a clean and sustainable method for green fuel.[1-4] Many semiconductor-based materials have been tested as photocatalysts for water-splitting to generate H_2. Upon irradiation of a photocatalyst, electron/hole pairs (excitons) are generated, each able to participate in redox reactions. While the photogenerated electrons promote the H_2 evolution reaction (HER), the oxygen (O_2) evolution reaction (OER) can utilize holes to produce O_2.[5-6] Overall water splitting involves the production of both H_2 and O_2, but it can suffer from slow kinetics due to the O_2 half-reaction, which requires at least four holes, compared to the HER, which only requires two electrons. To overcome this challenge, sacrificial electron donors such as triethylamine (TEA) and triethanolamine (TEOA) are used to suppress the OER and accelerate the HER.[7] Although this strategy can lead to high H_2 evolution rates (exceeding 2000 μmol h^{-1} g^{-1})[8], sacrificial electron donors are themselves valuable products, and the H_2 generated from their oxidation does not compensate for the energy required to produce them.[9-10] Therefore, it is desirable to take advantage of the oxidizing nature of the photogenerated holes to break down pollutants or produce valuable end products. A promising solution is designing a dual-functional photoredox system that can simultaneously utilize both the electrons and holes.

Dual-functional photocatalysis (DFP) couples the production of H_2 with the oxidation of organic molecules (i.e., organic synthesis), enabling the utilization of both photogenerated species (Figure 1).[9, 11-13] For instance, TiO_2 has been applied in concurrent H_2 production (180 μmol h^{-1} g^{-1}) and dehydrogenative lactonization of 1,2-benzenedimethanol, with a phthalide yield of 90%.[14] Although some progress has been made in understanding the underlying mechanisms of DFP, it is still unclear how to

maximize the output of both half-reactions simultaneously.[12] Without guidance on tuning the activity and selectivity of semiconductors for DFP, most of the studies reported are based on a trial-and-error approach.[11-12] Therefore, assessing the fundamental processes in DFP becomes crucial in designing efficient dual-functional photocatalysts.

After generating the electron/hole pairs, it is vital to transfer these charge carriers to the reactants (water and an organic molecule) with minimal energy loss. Energy loss can be due to charge recombination, the formation of a deep trap state, or multiple intermediate energy dissipation steps within or between different excited states. Femtosecond transient absorption (fs-TA) spectroscopy can be used to gain insights into how the photogenerated charge carrier dynamics affect the overall charge transfer and energy usage.[15-17] As an ultrafast electronic spectroscopic technique, fs-TA employs a pump pulse and a time-delayed probe pulse to track the excited state dynamics with characteristic time constants. For example, the solvation-aided excited state stabilization could improve charge transfer efficiency, in accord with a blue-shifted excited-state absorption (ESA) peak.[18-19]

Notably, trap states within a material can also affect the charge carrier dynamics. A shallow trap allows electrons to be rapidly transferred to the reactant or surrounding solvent, affording high reaction rates. In contrast, a much longer lifetime may indicate the recombination of deeply trapped carriers, leading to energy loss and reduced charge transfer. Therefore, materials that possess fewer intermediate energy transfer steps and high charge transfer rates (e.g., with accessible charge carriers out of a shallow trap state) would be beneficial for efficient DFP.[19-23]

Meanwhile, the energies of both the valence band (VB) and conduction band (CB) of the photocatalyst, and their alignment/overlap with the highest occupied molecular orbital (HOMO) of the organic molecule, are critical for achieving thermodynamically favorable DFP reactions (Figure 1). For water reduction, the CB energy must be more negative than the reduction potential of H^+/H_2 (0.0 eV vs. Normal Hydrogen Electrode (NHE) at pH=0). For the oxidation of the organic molecule, the HOMO of the molecules needs to be less positive than the VB of the photocatalyst. Hence, proper alignment of the VB and CB of the photocatalyst with the HOMO of the organic molecule and the H_2 evolution potential is crucial in DFP to achieve high H_2 evolution and oxidation rates.[24]

The synergy between light absorption, charge dynamics, and band alignment must be considered for designing suitable DFP materials. Metal-organic frameworks (MOFs) with versatile structures and tunable physicochemical properties present an ideal platform for such a task. As photocatalytic materials, MOFs are theoretically superior to traditional semiconductors due to their: (i) high porosity, which allows co-catalysts and organic molecules to diffuse within them, increasing their interactions[22], and (ii) highly tunable structures that allow their optoelectronic properties, conductivity, and hydrolytic stability to be modified by changing the metal ions or functionalizing the organic ligand.[25-30] Moreover, traditional semiconductors are limited by their ability to primarily absorb UV light, whereas MOFs can be tuned to absorb visible light that represents a more significant fraction of solar energy reaching Earth. Hence, photocatalysts with a broader light absorption range can be useful in DFP.[26, 31]

MOFs have been previously applied in DFP, such as MIL-125-NH_2, which photodegraded Rhodamine B while producing H_2 at a rate of 335 μmol h^{-1} g^{-1}.[24] PCN-777 simultaneously generated H_2 (30 μmol h^{-1} g^{-1}) and oxidized benzylamine with 90%

selectivity.[32] Other examples of DFP include oxidizing water while reducing carbon dioxide (CO_2) or dinitrogen (N_2) to methanol (CH_4), or ammonia (NH_3), respectively.[33-34] The aforementioned reactions involve gases, making it challenging to determine their specific interactions with the MOF photocatalyst. We envision a DFP system where organic molecules can diffuse within the pore space and interact with localized holes on the organic linkers while the delocalized, photogenerated electrons can reduce water to H_2. Detailed studies on the underlying mechanisms are lacking, and the essential photophysical properties for MOFs to maximize DFP remain elusive.

In this work, we describe for the first time the impact of light absorption, charge carrier dynamics, and band alignment in MOFs for DFP. The fs-TA spectroscopy, computed Projected Density of States (PDOS), and computational predictions of bandgap alignments based on Density-Functional Theory (DFT) were used in concert to investigate the role of photogenerated charges within the MOF photocatalyst.[32, 35] Four zirconium-based MOFs (UiO-66 analogs) were synthesized using the functionalized terephthalic acid ligands: aminoterephthalic acid, 2,5-pyridinedicarboxylic acid (pd), and 2,5-pyrazinedicarboxylic acid (pz). Compared to terephthalic acid used in UiO-66, the pd and pz ligands have nitrogen (N) atoms in the aromatic ring. Each N-atom possesses a lone pair of electrons, resulting in higher electron density, enhanced electron delocalization, and conductivity, thereby benefitting DFP in general. The incorporation of N-atoms attached to or within the benzene ring alters the light absorption, bandgap, and charge transfer properties of each MOF. The UiO-66 analogs were employed in DFP, coupling water reduction for H_2 production with the oxidation of benzenethiol. The relationship between the photophysical properties of each MOF and their catalytic activity as dual-functional photocatalysts was elucidated.

Experimental Section

Materials. All the chemicals and solvents in this work were purchased from commercial sources and used without further purification.

Synthesis of UiO-66. A mixture of zirconium(IV) chloride (20 mg, 0.08 mmol) and benzoic acid (500 mg, 0.6 mmol) was dissolved in 5 mL dimethylformamide (DMF), followed by the addition and dissolution of terephthalic acid (11.4 mg, 0.06 mmol). The mixture was stirred to form a homogeneous solution, heated in a Pyrex vial at 120 °C for 72 h, and cooled to room temperature. The as-obtained products were filtered and washed with DMF (3×). Finally, the as-prepared UiO-66 powder was air-dried overnight.

Synthesis of UiO-66-NH_2. UiO-66-NH_2 was synthesized in a similar manner to UiO-66, except that 2-aminoterephthalic acid (12.4 mg, 0.06 mmol) was used instead of terephthalic acid.

Synthesis of UiO-66-pd. A mixture of zirconium(IV) chloride (143.4 mg, 0.6 mmol) and 2,5-pyridinedicarboxylic acid (73.3 mg, 0.4 mmol) was dissolved in 4.5 mL formic acid and 0.5 mL deionized (DI)-water. The mixture was treated with ultrasound for 20 minutes to form a homogeneous solution, then heated in a Pyrex vial at 120 °C for 3 h and cooled to room temperature. The suspension was separated by centrifugation and washed with DI-water and ethanol. The product was dried under ambient conditions.

Synthesis of UiO-66-pz. UiO-66-pz was synthesized in a similar manner to UiO-66-pd, except that 2,5-pyrazinedicarboxylic acid (89.5 mg, 0.4 mmol) was used instead of 2,5-pyridinedicarboxylic acid.

Results and Discussion

Synthesis and Characterization. The UiO-66 ($Zr_6O_4(OH)_4(BDC)_6$, where BDC= terephthalic acid) family of MOFs was selected in this study due to their thermal and hydrolytic stability. UiO-66 analogs can be synthesized using different dicarboxylate ligands while retaining structural morphology[36]; we synthesized UiO-66 analogs using three different N-functionalized ligands: 2-aminoterephthalic acid (UiO-66-NH_2), 2,5-pyridinedicarboxylic acid (pd) (UiO-66-pd), and 2,5-pyrazinedicarboxylic acid (pz) (UiO-66-pz) (Figure 2a). The 2-aminoterephthalic acid has a $–NH_2$ group attached to the aromatic ring. The pd and pz ligands have one and two N-atoms in the within the aromatic ring, respectively. Each functionalized MOF has the same cubic structure as UiO-66, crystallizing in the space group *Fm-3m* and possessing **fcu** topology.[37] The secondary building units (SBUs) of each MOF are composed of cuboctahedral zirconium-oxide clusters with the formula $Zr_6O_4(OH)_4$, and each SBU is 12-connected to the functionalized terephthalic acid linkers through their carboxylate groups.[37-38] Powder X-ray diffraction (PXRD) patterns confirmed that these MOFs are crystalline, isostructural, and phase pure (Figure 2b). Nitrogen (N_2) isotherms collected at 77 K and 1 bar revealed that all MOFs are microporous with Brunauer–Emmett–Teller (BET) surface areas of 734, 705, 678, and 679 m^2/g for UiO-66, UiO-66-NH_2, UiO-66-pd, and UiO-66-pz, respectively (Figure 2c). Scanning electron microscopy (SEM) images showed that all the MOFs have similar octahedral crystal morphologies (Figure S1). Thermogravimetric analysis (TGA) showed that all UiO-66 analogs are stable up to 300 °C. The mass loss of all the MOF before 300 °C was correlated to the removal of guest solvent molecules residing within the pores of the MOFs. The mass loss of all the MOF at 300 °C or above this temperature is due to the structure collapsing of the MOF (Figure S2). Electrochemical Impedance Spectroscopy (EIS) was used to determine the electrical conductivity of each MOF. A Nyquist plot designates low charge-transfer

resistance when the radius of the semi-circle formed is small[20, 39-40], meaning that the charge carriers can migrate more freely through the MOF and participate in redox reactions. In the Nyquist plot (Figure 2d), UiO-66-pz has the lowest charge-transfer resistance, followed by UiO-66-pd, UiO-66-NH_2, and UiO-66. The EIS data reveal that the additional electron lone pair(s) provided by N atoms in the aromatic ring increases the MOF conductivity.

Photophysical Properties. Ultraviolet-visible (UV-vis) spectroscopy and calculated PDOS were utilized to characterize the light-harvesting properties of each MOF. UiO-66-NH_2 shows an absorption band up to 430 nm, attributable to the amino-functionalized ligand acting as a photosensitizer.[41] In contrast to the similar absorption edges (335 nm) of UiO-66 and UiO-66-pd with one N-atom in the aromatic ring (Figure 2e), the notably extended absorption edge of UiO-66-pz to 380 nm implies that two N-atoms in the aromatic ring affects the light-harvesting capabilities. The enhanced electron-donating properties of the N-heterocycle in UiO-66-pz red-shift the absorption from UiO-66 and UiO-66-pd. The bandgap for each MOF was calculated from the diffuse reflectance spectroscopy data[42], with UiO-66-NH_2 (2.88 eV) and UiO-66-pz (3.24 eV) having smaller band gaps than UiO-66 (3.84 eV) and UiO-66-pd (3.89 eV) (Figure 2e, Figure S3). The smaller bandgap of UiO-66-NH_2 and UiO-66-pz implies that less energy is required to generate charge carriers when compared to UiO-66 and UiO-66-pd.

The computed PDOS revealed that the N *p*-orbitals in UiO-66-pd and UiO-66-pz and the C *p*-orbitals in UiO-66-NH_2 contribute most to the states close to the valence band maximum (Figure S4). The Ultra p X-ray photoelectron spectroscopy (XPS) revealed that the energy levels of the valence bands for UiO-66-pd and UiO-66-pz are 2.39 and 1.79 eV respectively (Figure S5). The valence states close to the band gap are mostly

ligand in character, dominated by the N and C *p*-orbitals, whereas the conduction bands have a mixture of ligand N(*p*) and C(*p*) and Zr *d*-orbitals. Calculations reveal that the substitutions in the N-containing MOFs have the effect of pushing occupied localized ligand states between the Highest Occupied Crystal Orbital (HOCO) and Lowest Unoccupied Crystal Orbital (LUCO) of UiO-66, which narrows their respective band gaps.

The localization of the electrons and holes in each MOF structure was determined using the DFT-calculated isodensity surfaces of the HOCO and LUCO for the hole and electron, respectively (Figure 3). The photogenerated electrons in all four MOFs were primarily located on the ligand. The holes of UiO-66-NH_2, UiO-66-pd, and UiO-66-pz are mainly situated on the ligand of each MOF. In contrast, the holes of UiO-66 are spatially positioned on the nodal and linker O atoms, which differs from the location of the electrons, thus leading to lower exciton binding energy and better hole mobility (but reduced charge transfer capabilities, see fs-TA results below). Notably, the N-functionalized ligands seem to exert a more significant impact on the location of holes than that of the electrons.

Fs-TA experiments were performed on all four MOFs to elucidate the excited-state electronic dynamics governing the subsequent redox reactions (Figure 4).[19] All four MOFs exhibit a broad ESA band: UiO-66 and UiO-66-NH_2 show a narrow band centered at ~598 and 630 nm, respectively; UiO-66-pd shows a bluer broad band centered at ~520 nm, while UiO-66-pz displays two maxima at 515 and 575 nm. Since the TA kinetics are generally affected by spectral overlap, global analysis was performed to retrieve the characteristic time constants of the excited state decay, which can be best fit using four components. Under UV excitation, the solvent (acetonitrile) shows a weak TA signal that decays completely within 1 ps; therefore, we can assign

the first time constant (τ_1) to Franck–Condon relaxation of the MOFs convoluted with the solvent response.

The τ_2 component exhibits a clear blueshift of the ESA peak of UiO-66-pd and UiO-66-pz, whereas in UiO-66-NH_2, there is a much smaller frequency shift and primarily an intensity change. Interestingly, UiO-66 shows a small redshift on this timescale, which may be due to a rapidly decaying blue shoulder of the ESA band that is broader (more heterogeneous) than that in UiO-66-NH_2. As depicted on the excited-state potential energy surface (Figure 4a), τ_2 corresponds to ultrafast stabilization of the excited state by solvation (i.e., reorientation of solvent molecules afforded by the MOFs' porosity), which may facilitate the exciton dissociation and charge transfer from the ligand to a trap state. The pertinent time constant of ~2–5 ps is larger than the ~1 ps exciton dissociation time observed in perovskites such as $FAPbI_3$[43], consistent with a higher exciton binding energy in these MOFs. Moreover, due to different structural defects, the intrinsically heterogeneous MOF structure could provide trap states that prime the system for separating and transferring the photogenerated charge carriers.[20] A similar transition has been observed for zirconium-based MOFs with naphthalene dicarboxylate ligands, where the transition was assigned to a ligand-to-cluster charge transfer mechanism with the formation of a charge-separated state.[19, 44] Regardless of the exact nature of the product state, an ultrafast energy stabilization is achieved on the few ps timescale so that charge carriers emerge mainly in association with a shallow trap state.

Notably, τ_3 and τ_4 represent the majority of ESA intensity decay (80–90%) and are most relevant to the redox performance of UiO-66 analogs. In general, a long-lived excited state is beneficial for DFP with more time for the excited state potential to be harvested

for catalysis. However, the longest lifetime of τ_4 shows only a slight variation between samples from ~690 ps (UiO-66-NH_2) to 900 ps (UiO-66), which cannot be the main factor explaining the performance differences between these materials. We can attribute it to the recombination of trapped carriers from deep trap states that are less accessible for reduction (Figure 4a).[20, 45] However, even though the deep-trapped electrons may not be readily available for reduction reactions, the corresponding holes could become available for oxidation reactions, and the largest t4 in UiO-66 is in accord with its greater hole mobility and the best oxidation potential among all the MOFs tested (see below).

In contrast, τ_3 shows a clear change between UiO-66/UiO-66-NH_2 (~55 ps) and UiO-66-pd/UiO-66-pz (~100 ps). This notable and consistent difference indicates that the different electronic landscape with the pd and pz ligands imposes a slower relaxation step on the ultrafast timescale, which is likely associated with a shallow trap state of MOF that plays an important role in charge transfer. In other words, the prolonged lifetime of shallow-trapped electrons is a major distinction from UiO-66-NH_2 and is the result of N atoms within the benzene ring of the pd and pz ligands. If these shallow-trapped electrons are accessible for photocatalysis, the longer lifetime becomes a significant benefit. Nevertheless, there is a wide temporal gap between these primary events (fs–ps) and the oxidation reactions (μs–s) downstream, which may require further investigations to track the electronic dynamics after the system moves out of the trap states beyond the ligands, and under more realistic catalytic conditions.

To delineate the contribution of ligands to the overall MOF signal, TA was performed on the bare ligands (Figure S6b,c). The high similarity between the ligand and MOF TA profiles indicates that the conduction band has considerable ligand character, in

agreement with PDOS calculations (Figure S4b). The excited state lifetime of the pd ligand is considerably shorter than that of the corresponding MOF, suggesting that interactions with the metal nodes and close packing of organic linkers lead to a prolonged excited state population (e.g., a long-lived trap state).

Previous literature reported that pristine UiO-66-NH_2 has a very short excited-state lifetime (~1.5 ps), while samples with missing linker defects show a significantly longer excited state lifetime (~150 ps).[46] Enhanced ligand-to-metal charge transfer (LMCT) character can arise from structural defects (e.g., missing linkers), which shrink the energy gap between the ligand LUMO and metal *d*-orbitals in the MOF. Past a critical concentration of defects, the excited state lifetime increases dramatically to the ns timescale, which is thought to correspond to deeply trapped electrons that cannot be utilized for photocatalysis. Overall, our TA data imply that all four MOFs contain considerable defects that prolong the excited state lifetimes to hundreds of ps and facilitate charge transfer, which can benefit HER.

Hydrogen Evolution Half-Reaction. After examining each MOF's photophysical properties, we turned next to their photocatalytic performance for H_2 evolution. The H_2 generation experiments were performed using a 305 nm cut-off filter, triethylamine (TEA) as the sacrificial electron donor, and Pt NPs as the co-catalyst (Figure S7, Table S1). Upon addition of the Pt NPs with UiO-66 or UiO-66-NH_2, our TA results show that there is a lifetime decrease with τ_4 showing the largest change from 900 to 560 ps in UiO-66 (Figure S6a) and from 690 to 370 ps in UiO-66-NH_2 (Figure S6b). In contrast, the TA signals for UiO-66-pd and UiO-66-pz are diminished with Pt NPs due to destabilization of the MOF suspension. This finding of a shortened excited state lifetime is in accord with the observed photoluminescence (PL) quenching after mixing

Pt NPs with the MOFs (Figure S8). The TA and PL results confirm that Pt NPs attract the electron from the MOFs, decreasing the rate of undesired charge recombination.[24] The photocatalytic reaction conditions were optimized by varying the concentrations of MOF photocatalysts, TEA, and Pt NPs. After optimization, the Pt/UiO-66-NH_2 photocatalytic system showed the highest H_2 evolution rate of ~300 μmol h^{-1} g^{-1}, followed by Pt/UiO-66-pz and Pt/UiO-66-pd achieving 153 and 97 μmol h^{-1} g^{-1}, respectively. Pt/UiO-66 was inferior to the other MOFs, displaying the lowest H_2 evolution rate of 34 μmol h^{-1} g^{-1} (Figure S9). UiO-66-NH_2 and UiO-66-pz possess smaller bandgaps than UiO-66 and UiO-66-pd, permitting more effective light-harvesting and leading to higher H_2 evolution rates. The stability of each MOF post-irradiation was confirmed using PXRD, which showed the preserved crystallinity of each MOF, and the material could be reused without losing catalytic efficiency (Figure S10).

Dual-Functional Photocatalytic Activity. To take advantage of both the photoexcited electrons and holes, we replaced the sacrificial electron donor TEA with benzenethiol, envisioning simultaneous production of H_2 and synthesis of sulfide-based products. The oxidation of thiols has been widely used to synthesize sulfide-based products[47-48], which are essential compounds in biological (drugs synthesis, DNA cleavage)[49] and industrial applications (rubber vulcanization and rechargeable lithium batteries).[50] Therefore, it would be advantageous to develop a dual-functional photocatalytic system that could generate H_2 fuel and concurrently synthesize value-added sulfide-based products (Figure 5a). In the dual-functional reaction, Pt/UiO-66-pz exhibits the highest H_2 evolution rate of 329±13 μmol h^{-1} g^{-1}, followed by Pt/UiO-66-NH_2 and Pt/UiO-66-pd with rates of 146±2 and 102±16 μmol h^{-1} g^{-1}, respectively. Pt/UiO-66 shows the

lowest H_2 evolution rate of 55±4 μmol h^{-1} g^{-1} (Figure 5a). After the photocatalytic reaction, all the MOFs maintained their crystallinity (Figure S11).

To determine the efficiency of the oxidation half-reaction, the conversion yield of benzenethiol to sulfide-based products was quantified by UV-vis spectroscopy using Ellman's Reagent (dithionitrobenzoic acid, DTNB) [51] (Figure S12). The DTNB peak intensity at ~410 nm shows the largest decrease for Pt/UiO-66 (Figure 5b), signifying the largest conversion of benzenethiol to sulfide-based products (75.9%), followed by Pt/UiO-66-pz and Pt/UiO-66-NH_2 with yields of 70.4% and 53.5%, respectively. Pt/UiO-66-pd exhibits the lowest yield at 36.5% compared to the other MOFs. The large conversion displayed by UiO-66 is likely from the spatial separation of the holes and electrons in the UiO-66 structure. According to the isodensity surfaces (Figure 3), the holes are confined to the metal nodes while the electrons are located on organic ligands. This spatial separation could decrease recombination rates and afford greater hole mobility, benefitting the oxidation of benzenethiol half-reaction at the expense of H_2 production. In addition to UV-vis spectroscopy, gas chromatography-mass spectrometry (GC-MS) was used to qualitatively and quantitatively evaluate the sulfide-based products with Pt/UiO-66-pz. GC-MS data showed that although our dual-functional photocatalyst Pt/UiO-66-pz is not selective in the production of diphenyl disulfide, it can readily oxidize benzenethiol to produce sulfide-based products while simultaneously producing H_2 (Figure S13).

The same photocatalytic reaction setup with only Pt NPs and no MOF photocatalyst showed a lower H_2 evolution rate of 0.75 μmol h^{-1} (4.94 μmol h^{-1} for Pt/UiO-66-pz) and sulfide-based products yield of 25.7%, demonstrating that the MOFs are vital for the photocatalytic system to achieve high H_2 evolution rates and benzenethiol conversion. Moreover, when the photocatalytic reaction was carried out with D_2O

instead of DI-water, Pt/UiO-66-pz had an H_2 evolution rate that was three times lower, signifying that the H_2 being produced arises from both water (234 μmol h^{-1} g^{-1}, ~71%) and dehydrocoupling of the thiols (95 μmol h^{-1} g^{-1}, ~29%) (Figure S14).[48, 52]

The photocatalytic reaction was also tested using different wavelengths of light and different temperatures under different experimental conditions. When a 360 nm light cut-off filter was used, Pt/UiO-66-pz showed a poor H_2 evolution rate and sulfide-based products yield (<0.5 μmol h^{-1} g^{-1}, ~23.3%) (Figure S15). Above 360 nm, UiO-66-pz showed minimal light absorption, and could not efficiently utilize it for photocatalysis. To test for temperature affects, the same reaction setup was used but instead of irradiating the material, it was place in a 60˚C water bath for the same reaction time. Under these conditions, Pt/UiO-66-pz had a H_2 evolution rate of <0.5 μmol h^{-1} g^{-1} and ~22.2% sulfide-based products yield (Figure S16), demonstrating that the contribution from temperature was negligible in driving the photocatalytic reaction. Overall, Pt/UiO-66-pz performs best in the coupled redox system, achieving the highest H_2 production rate of ~329 μmol h^{-1} g^{-1} while oxidizing 70.4% of benzenethiol (Figure 5).

Holes and reactive oxygen species (ROS) are the primary active species responsible for the photocatalytic oxidation of organic molecules.[53] To elucidate the active species governing the oxidation of benzenethiol, the hole scavenger triethanolamine (TEOA) and the hydroxyl radical (•OH) scavenger tert-butanol (tBuOH) were used individually with Pt/UiO-66-pz in the same photocatalytic setup.[24] Upon adding TEOA, Pt/UiO-66-pz exhibits an H_2 evolution rate of 233 μmol h^{-1} g^{-1} and a 62.7% yield of sulfide-based products, slightly lower than the DFP reaction without a scavenger (Figure 5a, b). Upon adding tBuOH, the hydrogen evolution rate (173 μmol h^{-1} g^{-1}) and sulfide-based products yield (28.6%) decreased significantly. These results confirm that both the holes and hydroxyl radicals are involved in the oxidation of benzenethiol to sulfide-

based products, with hydroxyl radicals being the dominant reactive species (Figure S17).

To gain further insights into the effect of benzenethiol substituents on both the reduction and oxidation half-reactions, we replaced benzenethiol with 4-chlorobenzenethiol, which contains an electron-withdrawing chlorine (Cl) atom. In the same DFP reaction setup using Pt/UiO-66-pz, we observed a decrease in the H_2 evolution rate (156 μmol h^{-1} g^{-1}) and sulfide-based products yield (36.5%) compared to the DFP reaction with benzenethiol (Figure S18). The HOMO of 4-chlorobenzenethiol is slightly lower than that of benzenethiol, representing a smaller thermodynamic driving force for hole transfer (Figure S19). Moreover, the lower conversion of 4-chlorobenzenethiol could stem from the deactivating nature of halogens in electrophilic aromatic substitution reactions.[54-55] Assuming that the reaction proceeds via a thiyl radical[48, 56], the Cl-substituent can deactivate the aromatic ring of one radical, making it less susceptible to electrophilic attack by another thiyl radical[57], and thereby decreasing the overall reactivity and yield. Despite the reduced yield, Pt/UiO-66-pz is selective in producing bis(dichlorophenyl)disulfide, and the dual-functional reaction is still successful. This demonstrates that the dual-functional nature of Pt/UiO-66-pz is not limited to a single type of benzenethiol reactant.

Conclusions

Dual-functional photocatalysis enables the utilization of both the photogenerated electrons and holes, elevating the photocatalytic system beyond the competition for high H_2 production rates and enhancing its utility without the need for sacrificial reagents such as TEA. This work employed four MOFs (UiO-66 analogs) with N-functionalized ligands in a dual-functional photocatalytic reaction. The number and

position of the N-atoms attached to or within the benzene ring correlate to the photophysical (light absorption, bandgap, and excited state dynamics) and electronic (conductivity) properties of each MOF. We demonstrated that the presence of the N-atoms in the ligands effectively enhances the photophysical properties of MOFs toward efficient DFP.

The Pt/UiO-66-pz manifests the highest H_2 evolution rate and the second-best benzenethiol conversion. Compared to other MOFs, the higher performance of UiO-66-pz can be attributed to an ultrafast energy stabilization step (~4 ps) toward a shallow trap state (~95 ps lifetime) to facilitate charge transfer, a relatively small bandgap (3.1 eV), and high conductivity. Although the structure and functionality of UiO-66-pd was closely similar to UiO-66-pz, the lower absorption range and electron conductivity of UiO-66-pd leads to the poorer performance on both H_2 evolution rate and the benzenethiol conversion. In contrast, UiO-66 performs the best in benzenethiol conversion (75.9%) due to the spatial separation of electrons and holes but is the worst photocatalyst for H_2 generation due to its wider bandgap, lower conductivity, and short excited-state lifetime. Thus, MOFs for DFP need a moderately small bandgap that straddles the water oxidation and reduction potentials, a VB that is below the HOMO of the organic molecule, high conductivity, and shallow trap states that allow for longer (~100 ps) excited state lifetimes. Our work has improved our understanding of the interplay of each of these features, allowing for the design and development of more efficient dual-functional photocatalytic MOFs through careful consideration of each of these parts.

Our study characterizes the photophysical properties that underlie highly efficient DFP, especially for Pt/UiO-66-pz, wherein both the production of H_2 and synthesis of organic molecules can be achieved simultaneously. With the deepened mechanistic insights

from ultrafast exciton dissociation, charge transfer, and predictive knowledge about frontier orbitals containing ligand π* and metal *d*-orbitals, we envision future rational design of MOFs to optimize the yield and selectivity of dual-functional photocatalytic reactions. A potential design route is to further red-shift the absorption of N heterocycles using electron-donating substituents (e.g., $–NH_2$, –OH) or extending the ligand structure with dipyrazine ligands. The enhanced excited-state relaxation pathway out of a shallow-trap state could be coupled with a broader absorption profile to maximize the DFP performance, augmented by fine-tuning the HOCO-LUCO alignment for these new N-heterocyclic MOFs.

Supporting Information

The Supporting Information is available free of charge at https://xxx. Experimental methods, femtosecond transient absorption, computational methods, photocatalysis experiments and analysis are provided in the Supporting Information.

Author Contributions

K.C.S. conceived the project and designed the experiments together with N.C.C., and M.T.N. N.C.C. led the experimental work. N.C.C. and M.T.N. performed the DFP experiments and interpreted the data. S.K.W. synthesized the materials used for DFP. L.T., L.S.L., and C.F. performed the transient absorption experiments and analyzed the data. J.S.H. and T.Z. led the theoretical calculations described in this work. E.M.H. and K.G. analyzed the oxidation products formed after DFP. All authors contributed to the writing and editing of the manuscript.

Acknowledgements

K.C.S. thanks the Department of Chemistry at Oregon State University (OSU) for support through start-up funding and the College of Science SciRIS-II grant (2021). C.F. acknowledges the NSF grant CBET-2038381. T.J.Z. acknowledges support through Oregon State University (OSU) start-up funding. M.T.N. and N.C.C. acknowledge support from the Department of Chemistry for their Milton Harris and David P. & Clara B. Shoemaker Graduate fellowships respectively. The authors thank Dr. Yunkai Xu for help in the collection of EIS data and Dr. Marilyn Mackiewicz for useful discussions.

References

1. Zou, X.; Zhang, Y., Noble metal-free hydrogen evolution catalysts for water splitting. *Chem. Soc. Rev.* **2015,** *44* (15), 5148-80.

2. Pan, L.; Liu, Y.; Yao, L.; Dan, R.; Sivula, K.; Gratzel, M.; Hagfeldt, A., Cu_2O photocathodes with band-tail states assisted hole transport for standalone solar water splitting. *Nat. Commun.* **2020,** *11* (1), 318.

3. Nam, D. H.; Zhang, J. Z.; Andrei, V.; Kornienko, N.; Heidary, N.; Wagner, A.; Nakanishi, K.; Sokol, K. P.; Slater, B.; Zebger, I.; Hofmann, S.; Fontecilla-Camps, J. C.; Park, C. B.; Reisner, E., Solar Water Splitting with a Hydrogenase Integrated in Photoelectrochemical Tandem Cells. *Angew. Chem. Int. Ed.* **2018,** *57* (33), 10595-10599.

4. Banerjee, T.; Gottschling, K.; Savasci, G.; Ochsenfeld, C.; Lotsch, B. V., H_2 Evolution with Covalent Organic Framework Photocatalysts. *ACS Energy Lett.* **2018,** *3* (2), 400-409.

5. Chen, S.; Takata, T.; Domen, K., Particulate photocatalysts for overall water splitting. *Nat. Rev. Mater.* **2017,** *2* (10), 17050.

6. Reece Steven, Y.; Hamel Jonathan, A.; Sung, K.; Jarvi Thomas, D.; Esswein Arthur, J.; Pijpers Joep, J. H.; Nocera Daniel, G., Wireless Solar Water Splitting Using Silicon-Based Semiconductors and Earth-Abundant Catalysts. *Science* **2011,** *334* (6056), 645-648.

7. Luo, N.; Montini, T.; Zhang, J.; Fornasiero, P.; Fonda, E.; Hou, T.; Nie, W.; Lu, J.; Liu, J.; Heggen, M.; Lin, L.; Ma, C.; Wang, M.; Fan, F.; Jin, S.; Wang, F., Visible-light-driven coproduction of diesel precursors and hydrogen from lignocellulose-derived methylfurans. *Nat. Energy* **2019,** *4* (7), 575-584.

8. Wang, Z.; Yang, X.; Yang, T.; Zhao, Y.; Wang, F.; Chen, Y.; Zeng, J. H.; Yan, C.; Huang, F.; Jiang, J.-X., Dibenzothiophene Dioxide Based Conjugated Microporous Polymers for Visible-Light-Driven Hydrogen Production. *ACS Catal.* **2018,** *8* (9), 8590-8596.

9. Rahman, M. Z.; Edvinsson, T.; Gascon, J., Hole utilization in solar hydrogen production. *Nat. Rev. Chem.* **2022,** *6* (4), 243-258.

10. Schneider, J.; Bahnemann, D. W., Undesired Role of Sacrificial Reagents in Photocatalysis. *J. Phys. Chem. Lett.* **2013,** *4* (20), 3479-3483.

11. Qi, M. Y.; Conte, M.; Anpo, M.; Tang, Z. R.; Xu, Y. J., Cooperative Coupling of Oxidative Organic Synthesis and Hydrogen Production over Semiconductor-Based Photocatalysts. *Chem. Rev.* **2021,** *121* (21), 13051-13085.

12. Kampouri, S.; Stylianou, K. C., Dual-Functional Photocatalysis for Simultaneous Hydrogen Production and Oxidation of Organic Substances. *ACS Catal.* **2019,** *9* (5), 4247-4270.

13. Kasap, H.; Caputo, C. A.; Martindale, B. C.; Godin, R.; Lau, V. W.; Lotsch, B. V.; Durrant, J. R.; Reisner, E., Solar-Driven Reduction of Aqueous Protons Coupled to Selective Alcohol Oxidation with a Carbon Nitride-Molecular Ni Catalyst System. *J. Am. Chem. Soc.* **2016,** *138* (29), 9183-92.

14. Wada, E.; Tyagi, A.; Yamamoto, A.; Yoshida, H., Dehydrogenative lactonization of diols with a platinum-loaded titanium oxide photocatalyst. *Photochem. Photobiol. Sci.* **2017,** *16* (12), 1744-1748.

15. Krueger, T. D.; Solaris, J.; Tang, L.; Zhu, L.; Webber, C.; Van Court, R. C.; Robinson, S. C.; Ostroverkhova, O.; Fang, C., Illuminating Excited-State Intramolecular Proton Transfer of a Fungi-Derived Red Pigment for Sustainable Functional Materials. *J. Phys. Chem. C* **2021,** *126* (1), 459-477.

16. Tang, L.; Wang, Y.; Zhu, L.; Lee, C.; Fang, C., Correlated Molecular Structural Motions for Photoprotection after Deep-UV Irradiation. *J. Phys. Chem. Lett.* **2018,** *9* (9), 2311-2319.

17. Chuang, C.-H.; Lo, S. S.; Scholes, G. D.; Burda, C., Charge Separation and Recombination in CdTe/CdSe Core/Shell Nanocrystals as a Function of Shell Coverage: Probing the Onset of the Quasi Type-II Regime. *J. Phys. Chem. Lett.* **2010,** *1* (17), 2530-2535.

18. Yu, J.; Park, J.; Van Wyk, A.; Rumbles, G.; Deria, P., Excited-State Electronic Properties in Zr-Based Metal-Organic Frameworks as a Function of a Topological Network. *J. Am. Chem. Soc.* **2018,** *140* (33), 10488-10496.

19. Gutierrez, M.; Cohen, B.; Sanchez, F.; Douhal, A., Photochemistry of Zr-based MOFs: ligand-to-cluster charge transfer, energy transfer and excimer formation, what else is there? *Phys. Chem. Chem. Phys.* **2016,** *18* (40), 27761-27774.

20. Xiao, J.-D.; Shang, Q.; Xiong, Y.; Zhang, Q.; Luo, Y.; Yu, S.-H.; Jiang, H.-L., Boosting Photocatalytic Hydrogen Production of a Metal–Organic Framework Decorated with Platinum Nanoparticles: The Platinum Location Matters. *Angew. Chem. Int. Ed.* **2016,** *55* (32), 9389-9393.

21. Li, X.; Bi, W.; Zhang, L.; Tao, S.; Chu, W.; Zhang, Q.; Luo, Y.; Wu, C.; Xie, Y., Single-Atom Pt as Co-Catalyst for Enhanced Photocatalytic H_2 Evolution. *Adv. Mater.* **2016,** *28* (12), 2427-31.

22. Santiago Portillo, A.; Baldoví, H. G.; García Fernandez, M. T.; Navalón, S.; Atienzar, P.; Ferrer, B.; Alvaro, M.; Garcia, H.; Li, Z., Ti as Mediator in the Photoinduced Electron Transfer of Mixed-Metal NH_2–UiO-66(Zr/Ti): Transient Absorption Spectroscopy Study and Application in Photovoltaic Cell. *J. Phys. Chem. C* **2017,** *121* (12), 7015-7024.

23. Pan, Y.; Qian, Y.; Zheng, X.; Chu, S.-Q.; Yang, Y.; Ding, C.; Wang, X.; Yu, S.-H.; Jiang, H.-L., Precise fabrication of single-atom alloy co-catalyst with optimal charge state for enhanced photocatalysis. *Nat. Sci. Rev.* **2021,** *8* (1), nwaa224.

24. Kampouri, S.; Nguyen, T. N.; Spodaryk, M.; Palgrave, R. G.; Zuttel, A.; Smit, B.; Stylianou, K. C., Concurrent Photocatalytic Hydrogen Generation and Dye Degradation Using MIL-125-NH_2 under Visible Light Irradiation. *Adv. Funct. Mater.* **2018,** *28* (52), 9.

25. Han, S. Y.; Pan, D. L.; Chen, H.; Bu, X. B.; Gao, Y. X.; Gao, H.; Tian, Y.; Li, G. S.; Wang, G.; Cao, S. L.; Wan, C. Q.; Guo, G. C., A Methylthio-Functionalized-MOF Photocatalyst with High Performance for Visible-Light-Driven H_2 Evolution. *Angew. Chem. Int. Ed.* **2018,** *57* (31), 9864-9869.

26. Mohammadnezhad, F.; Kampouri, S.; Wolff, S. K.; Xu, Y.; Feyzi, M.; Lee, J.-H.; Ji, X.; Stylianou, K. C., Tuning the Optoelectronic Properties of Hybrid Functionalized MIL-125-NH_2 for Photocatalytic Hydrogen Evolution. *ACS Appl. Mater. Interfaces* **2021,** *13* (4), 5044-5051.

27. Hendon, C. H.; Tiana, D.; Fontecave, M.; Sanchez, C.; D'Arras, L.; Sassoye, C.; Rozes, L.; Mellot-Draznieks, C.; Walsh, A., Engineering the optical response of the titanium-MIL-125 metal-organic framework through ligand functionalization. *J. Am. Chem. Soc.* **2013,** *135* (30), 10942-5.

28. Nam, K. W.; Park, S. S.; Dos Reis, R.; Dravid, V. P.; Kim, H.; Mirkin, C. A.; Stoddart, J. F., Conductive 2D metal-organic framework for high-performance cathodes in aqueous rechargeable zinc batteries. *Nat. Commun* **2019,** *10* (1), 4948.

29. Noh, H.; Kung, C.-W.; Otake, K.-i.; Peters, A. W.; Li, Z.; Liao, Y.; Gong, X.; Farha, O. K.; Hupp, J. T., Redox-Mediator-Assisted Electrocatalytic Hydrogen Evolution from Water by a Molybdenum Sulfide-Functionalized Metal–Organic Framework. *ACS Catal.* **2018,** *8* (10), 9848-9858.

30. Chen, T.-F.; Han, S.-Y.; Wang, Z.-P.; Gao, H.; Wang, L.-Y.; Deng, Y.-H.; Wan, C.-Q.; Tian, Y.; Wang, Q.; Wang, G.; Li, G.-S., Modified UiO-66 frameworks with methylthio, thiol and sulfonic acid function groups: The structure and visible-light-driven photocatalytic property study. *Appl. Catal.* **2019,** *259*, 118047.

31. Liu, S.; Zhang, C.; Sun, Y.; Chen, Q.; He, L.; Zhang, K.; Zhang, J.; Liu, B.; Chen, L.-F., Design of metal-organic framework-based photocatalysts for hydrogen generation. *Coord. Chem. Rev.* **2020,** *413* (15), 213266.

32. Kohn, W.; Sham, L. J., Self-Consistent Equations Including Exchange and Correlation Effects. *Phys. Rev.* **1965,** *140* (4A), A1133-A1138.

33. Gutterød, E. S.; Lazzarini, A.; Fjermestad, T.; Kaur, G.; Manzoli, M.; Bordiga, S.; Svelle, S.; Lillerud, K. P.; Skúlason, E.; Øien-Ødegaard, S.; Nova, A.; Olsbye, U., Hydrogenation of CO_2 to Methanol by Pt Nanoparticles Encapsulated in UiO-67: Deciphering the Role of the Metal–Organic Framework. *J. Am. Chem. Soc.* **2020,** *142* (2), 999-1009.

34. Huang, H.; Wang, X.-S.; Philo, D.; Ichihara, F.; Song, H.; Li, Y.; Li, D.; Qiu, T.; Wang, S.; Ye, J., Toward visible-light-assisted photocatalytic nitrogen fixation: A titanium metal organic framework with functionalized ligands. *Appl. Catal.* **2020,** *267*, 118686.

35. Hohenberg, P.; Kohn, W., Inhomogeneous Electron Gas. *Phys. Rev.* **1964,** *136* (3B), B864-B871.

36. Kandiah, M.; Nilsen, M. H.; Usseglio, S.; Jakobsen, S.; Olsbye, U.; Tilset, M.; Larabi, C.; Quadrelli, E. A.; Bonino, F.; Lillerud, K. P., Synthesis and Stability of Tagged UiO-66 Zr-MOFs. *Chem. Mater.* **2010,** *22* (24), 6632-6640.

37. Winarta, J.; Shan, B.; McIntyre, S. M.; Ye, L.; Wang, C.; Liu, J.; Mu, B., A Decade of UiO-66 Research: A Historic Review of Dynamic Structure, Synthesis Mechanisms, and Characterization Techniques of an Archetypal Metal–Organic Framework. *Cryst. Growth Des.* **2020,** *20* (2), 1347-1362.

38. Valenzano, L.; Civalleri, B.; Chavan, S.; Bordiga, S.; Nilsen, M. H.; Jakobsen, S.; Lillerud, K. P.; Lamberti, C., Disclosing the Complex Structure of UiO-66 Metal Organic Framework: A Synergic Combination of Experiment and Theory. *Chem. Mater.* **2011,** *23* (7), 1700-1718.

39. Xu, M.; Li, D.; Sun, K.; Jiao, L.; Xie, C.; Ding, C.; Jiang, H. L., Interfacial Microenvironment Modulation Boosting Electron Transfer between Metal Nanoparticles and MOFs for Enhanced Photocatalysis. *Angew. Chem. Int. Ed.* **2021,** *60* (30), 16372-16376.

40. Zhang, C.; Lei, D.; Xie, C.; Hang, X.; He, C.; Jiang, H. L., Piezo-Photocatalysis over Metal-Organic Frameworks: Promoting Photocatalytic Activity by Piezoelectric Effect. *Adv. Mater.* **2021**, e2106308.

41. Horiuchi, Y.; Toyao, T.; Saito, M.; Mochizuki, K.; Iwata, M.; Higashimura, H.; Anpo, M.; Matsuoka, M., Visible-Light-Promoted Photocatalytic Hydrogen Production by Using an Amino-Functionalized Ti(IV) Metal–Organic Framework. *J. Phys. Chem. C* **2012,** *116* (39), 20848-20853.

42. Makula, P.; Pacia, M.; Macyk, W., How To Correctly Determine the Band Gap Energy of Modified Semiconductor Photocatalysts Based on UV-Vis Spectra. *J. Phys. Chem. Lett.* **2018,** *9* (23), 6814-6817.

43. Piatkowski, P.; Cohen, B.; Ponseca, C. S.; Salado, M.; Kazim, S.; Ahmad, S.; Sundström, V.; Douhal, A., Unraveling Charge Carriers Generation, Diffusion, and Recombination in Formamidinium Lead Triiodide Perovskite Polycrystalline Thin Film. *J. Phys. Chem. Lett.* **2016,** *7* (1), 204-210.

44. Wang, L.; Cai, M.; Sun, W.; He, L.; Zhang, X., Promoting Charge Separation in Semiconductor Nanocrystal Superstructures for Enhanced Photocatalytic Activity. *Adv. Mater. Interfaces* **2018,** *5* (13), 1701694.

45. Zhang, Q.; Luo, Y., Probing the ultrafast dynamics in nanomaterial complex systems by femtosecond transient absorption spectroscopy. *High Power Laser Sci. Eng.* **2016,** *4,* E22.

46. Nasalevich, M. A.; Hendon, C. H.; Santaclara, J. G.; Svane, K.; van der Linden, B.; Veber, S. L.; Fedin, M. V.; Houtepen, A. J.; van der Veen, M. A.; Kapteijn, F.; Walsh, A.; Gascon, J., Electronic origins of photocatalytic activity in d^0 metal organic frameworks. *Sci. Rep.* **2016,** *6*, 23676.

47. Dhakshinamoorthy, A.; Alvaro, M.; Garcia, H., Aerobic oxidation of thiols to disulfides using iron metal-organic frameworks as solid redox catalysts. *Chem. Commun.* **2010,** *46* (35), 6476-8.

48. Li, X.-B.; Li, Z.-J.; Gao, Y.-J.; Meng, Q.-Y.; Yu, S.; Weiss, R. G.; Tung, C.-H.; Wu, L.-Z., Mechanistic Insights into the Interface-Directed Transformation of Thiols into Disulfides and Molecular Hydrogen by Visible-Light Irradiation of Quantum Dots. *Angew. Chem. Int. Ed.* **2014,** *53* (8), 2085-2089.

49. Krishnan-Ghosh, Y.; Balasubramanian, S., Dynamic covalent chemistry on self-templating peptides: formation of a disulfide-linked beta-hairpin mimic. *Angew. Chem. Int. Ed.* **2003,** *42* (19), 2171-3.

50. Maddanimath, T.; Khollam, Y. B.; Aslam, M.; Mulla, I. S.; Vijayamohanan, K., Self-assembled monolayers of diphenyl disulphide: a novel cathode material for rechargeable lithium batteries. *J. Power Sources* **2003,** *124* (1), 133-142.

51. Ellman, G. L., Tissue sulfhydryl groups. *Arch. Biochem. Biophys.* **1959,** *82* (1), 70-77.

52. Xu, L.; Deng, X.; Li, Z., Photocatalytic splitting of thiols to produce disulfides and hydrogen over PtS/$ZnIn_2S_4$ nanocomposites under visible light. *Appl. Catal.* **2018,** *234*, 50-55.

53. Nosaka, Y.; Nosaka, A. Y., Generation and Detection of Reactive Oxygen Species in Photocatalysis. *Chem. Rev.* **2017,** *117* (17), 11302-11336.

54. Rosenthal, J.; Schuster, D. I., The Anomalous Reactivity of Fluorobenzene in Electrophilic Aromatic Substitution and Related Phenomena. *J. Chem. Ed.* **2003,** *80* (6), 679.

55. Munárriz, J.; Gallegos, M.; Contreras-García, J.; Martín Pendás, Á., Energetics of Electron Pairs in Electrophilic Aromatic Substitutions. *Molecules* **2021,** *26* (2), 513.

56. Tan, K. Y. D.; Teng, G. F.; Fan, W. Y., Photocatalytic Transformation of Organic and Water-Soluble Thiols into Disulfides and Hydrogen under Aerobic Conditions Using $Mn(CO)_5Br$. *Organometallics* **2011,** *30* (15), 4136-4143.

57. De Vleeschouwer, F.; Van Speybroeck, V.; Waroquier, M.; Geerlings, P.; De Proft, F., Electrophilicity and Nucleophilicity Index for Radicals. *Org. Lett.* **2007,** *9* (14), 2721-2724.

Figures

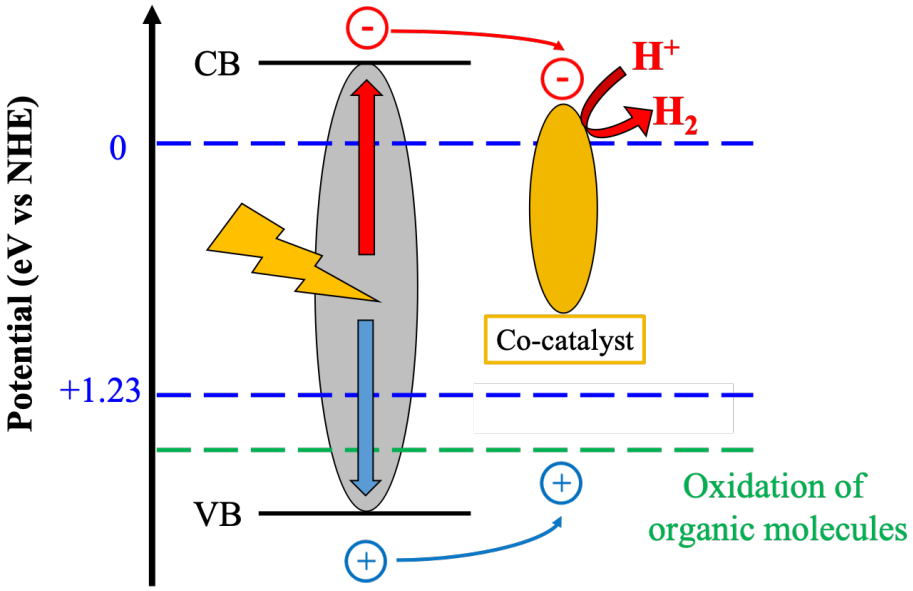

Figure 1. Schematic of a dual-functional photoredox system. Upon irradiation of the MOF, an electron is excited to the conduction band (CB) while a hole is left in the valence band (VB). The electrons in the CB of the photocatalyst are transferred to the co-catalyst (Pt NPs), which is responsible for reducing H^+ to H_2 (H^+/H_2, 0.0 eV vs. NHE). Meanwhile, the holes in the VB of the photocatalyst oxidize the organic molecule by moving to its HOMO.

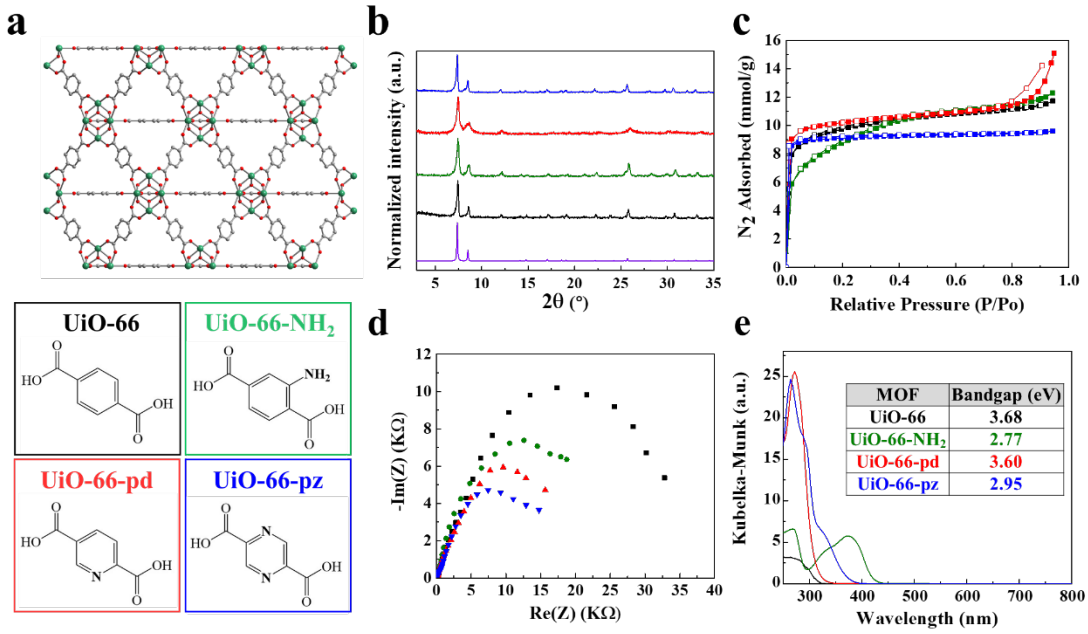

Figure 2. Structures and characterization of the four UiO-66 analogs. a) Representative structure of UiO-66 (top panel) and organic ligands used to synthesize four UiO-66 analogs, including terephthalic acid (black), 2-aminoterephthalic acid (green), 2,5-pyridinedicarboxylic acid (red), and 2,5-pyrazinedicarboxylic acid (blue). b) PXRD patterns of all four MOFs match the simulated UiO-66 PXRD pattern (purple), which can be synthesized as phase pure. c) Type-I N_2 isotherms collected for all MOFs at 77 K reveal that they are permanently porous and adsorb comparable amounts of N_2. d) EIS Nyquist plots reveal that UiO-66-pz has the smallest semi-circle radius, representing the lowest charge-transfer resistance. e) Kubelka–Munk transformation of the MOF's diffuse reflectance spectra collected from 250 to 800 nm. Inset: calculated bandgaps.

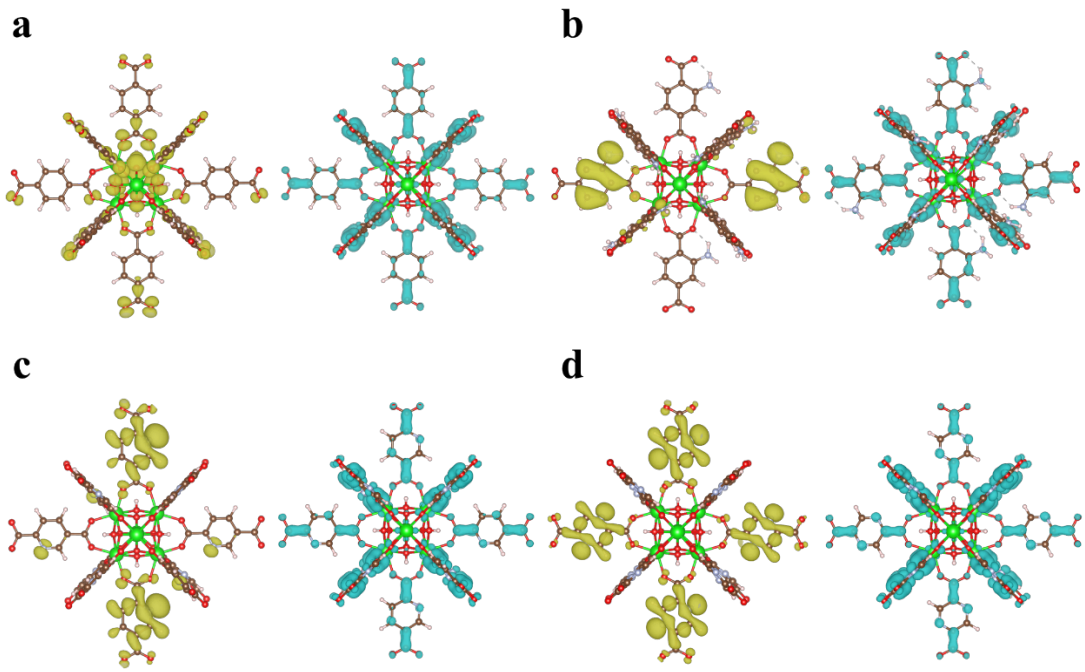

Figure 3. Electron-hole isodensity surfaces for the four UiO-66 analogs computed using density-functional theory (DFT). The $\rho_{h+}(r)$-region (yellow) represents hole accumulation, and the $\rho_{e-}(r)$-region (blue) indicates electron accumulation. The $\rho_{e-}(r)$-region for a) UiO-66, b) UiO-66-NH_2, c) UiO-66-pd, and d) UiO-66-pz, is comparable and located mainly on the ligand. The $\rho_{h+}(r)$-region of UiO-66 is positioned on the nodal and linker oxygens, whereas the $\rho_{h+}(r)$-region for UiO-66-NH_2, UiO-66-pd, and UiO-66-pz is positioned mostly on the ligand.

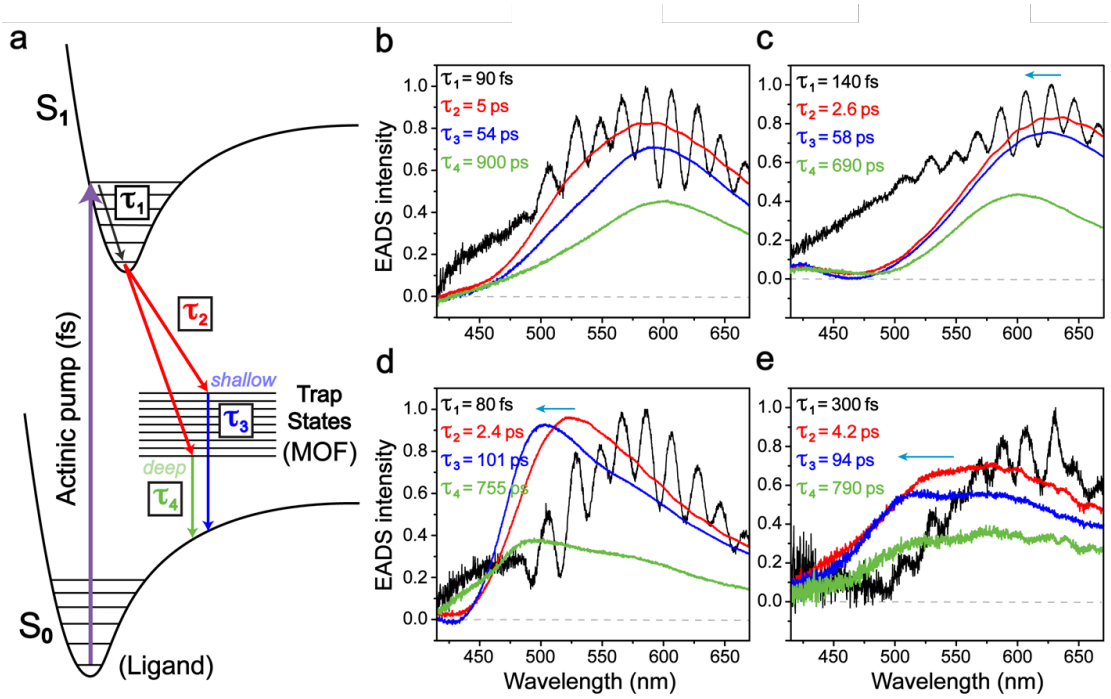

Figure 4. Transient electronic dynamics of the four UiO-66 analogs in suspension. a) Schematic of potential energy surfaces of the organic ligand and intermediate (both shallow and deep) trap states in MOFs. Key excited state energy relaxation pathways as primary events are depicted with the associated time constants (τ_1 to τ_4). Global analysis with a sequential kinetic model of the fs-TA spectra of b) UiO-66, c) UiO-66-NH_2, d) UiO-66-pd, and e) UiO-66-pz yields four characteristic lifetimes (listed in the insets): τ_1, black; τ_2, red; τ_3, blue; and τ_4, green for the evolution-associated difference spectra (EADS, normalized at the highest peak intensity for the initial black trace), which track the excited-state absorption (ESA) band dynamics. Except for UiO-66, a notable ESA peak blueshift on the few-ps timescale is depicted by cyan arrows in (**c**-**e**).

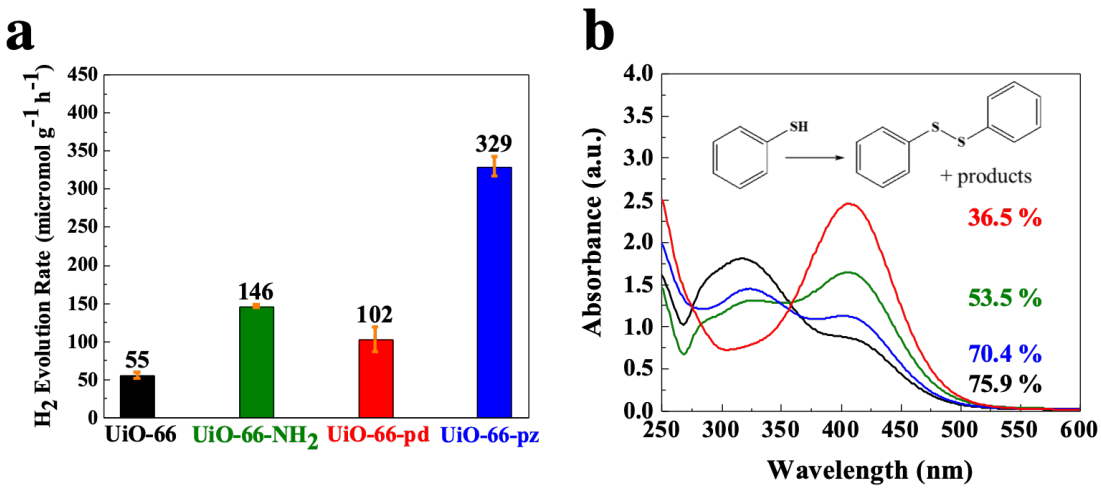

Figure 5. Dual-functional photocatalytic hydrogen generation and oxidation of benzenethiol. a) Comparison of H_2 evolution rates for UiO-66 (black), UiO-66-NH_2 (green), UiO-66-pd (red), and UiO-66-pz (blue) mixed with Pt NPs and 0.1 mL benzenethiol. b) UV-vis absorption spectra show the decrease of the DTNB peak at ~410 nm tracking the conversion to sulfide-based products with the best performance by Pt/UiO-66 (black), followed by Pt/UiO-66-pz (blue), Pt/UiO-66-NH_2 (green), and Pt/UiO-66-pd (red). The conversion yields were calculated using the calibration curve shown in Figure S20.

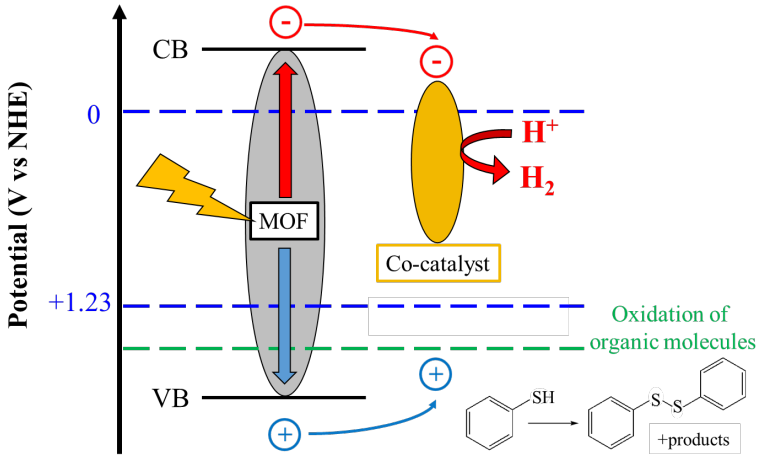
Potential (V vs NHE)
CB
0
+1.23
VB
MOF
Co-catalyst
H+
H2
Oxidation of
organic molecules
SH
S
S
+products

TOC Graphic